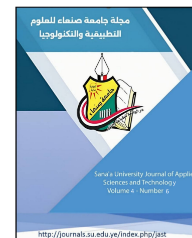

Studying Structural analysis by (X-ray and SEM) of (96.5-2x)Sn-(x)Ag-(3.5+x)Cu alloy with x =0.1,0.2,0.3,0.4 and 0.5 wt%

Hend. Q.A. Al-hubaishi *, A.H. Al-Hammadi , Ibrahim G.H. Loqman , Ahmed. M.A. Haider and Abdulmalek Mansoor N. Hulif

Department of Physics, Faculty of Sciences, Sana'a University, Sana'a, Yemen

*Corresponding author: h.alhubaishi@su.edu.ye

Abstract

In the pursuit of developing high-performance, lead-free solder alloys with enhanced reliability and environmental compliance, this study investigates the structural effects of incorporating the alloy (x)Ag–(3.5+x)Cu into the near-eutectic (96.5–2x)Sn system. The objective is to evaluate the influence of varying Ag and Cu concentrations on phase formation and microstructural evolution. Five alloy compositions were synthesized with x values of 0.1, 0.2, 0.3, 0.4, and 0.5 using conventional melting and casting techniques. The samples were characterized using X-ray diffraction (XRD) to identify crystalline phases and scanning electron microscopy (SEM) to analyze microstructural features. X-ray diffraction (XRD) analysis confirmed that all alloy samples predominantly consist of a single-phase tetragonal β-Sn structure. The incremental addition of silver and copper to the tin matrix enhanced the particle size refinement of the near-eutectic Sn–Ag–Cu ternary alloy. The introduction of the (x)Ag–(3.5+x)Cu alloy into the (96.5–2x)Sn system at varying concentrations (x = 0.1, 0.2, 0.3, 0.4, 0.5) resulted in noticeable shifts in diffraction peak positions (2θ), indicating lattice distortion and compositional changes. The calculated lattice parameters closely matched the standard peaks listed in JCPDS PDF No. 04-0673, and no new phases were detected within the ternary systems. Scanning electron microscopy (SEM) revealed distinct grayscale variations corresponding to differences in chemical composition and electron density across the microstructure. Notably, even minimal additions of Ag (x = 0.1) significantly improved the microstructural uniformity, which is critical for understanding the structural integrity and potential reliability of Sn–Ag–Cu solder joints in electronic interconnects.

Article Info

Keywords:
Sn-Ag-Cu alloy, lead-free solder, Structural Properties, Phases of interphase, (XRD), (SEM), (SEI).

Article History:
Received: 17-January-2026,
Revised: 6-March-2026,
Accepted: 1-June-2026,
Published: 28 June 2026.

1. INTRODUCTION

Soldering is a fundamental metallurgical joining process for metallic materials, in addition to alternative techniques such as fusion welding, brazing, diffusion bonding, and adhesive joining. In this process, a filler metal or alloy with a low melting temperature, generally below 315 ℃, is introduced to promote interfacial metallurgical interactions, enabling the formation of a stable and reliable joint without melting the base metals [1]. Joining conductors by soldering is one of the basic technologies in electronic circuit assembly, whereas advances in transistors, resistors, capacitors, diodes, and specially integrated circuits have revolutionized the world. These devices have very little value as individual components. For these devices to be used, they should be electrically connected to each other. Most of these electrical connectors are manufactured by soldering. The solder material does not only make electrical connections; In addition to its electrical function, it contributes to the mechanical interconnection of components and enhances the structural integrity of the printed circuit board, the joints in microelectronics serve to connect the two components mechanically, transfer the current across the joint and provide a path to dissipate heat from the packages [2]. The performance and quality of solders are important for the functioning of

different levels of electronic packaging, such as flip-chip connections, solder-ball connections in ball-grid arrays (BGA), or IC packing on printed circuit boards (PCB) [3]. Traditional eutectic tin-lead (Sn_{63}-Pb_{37}) or near-eutectic Sn_{60}-Pb_{40} alloys have been commonly used in packaging for a long time and have played a vital role in metal interconnection in the assembly of modern electronic circuits. The eutectic Sn_{63}-Pb_{37} solder has many advantages over other alloying elements, such as ease of handling, low melting temperature (183 ℃), good workability, ductility, and excellent wetting on copper and its alloys [4]. The presence of lead (Pb) in Sn-Pb solder alloys provides several technical advantages [5]. It decreases the melting temperature of Sn-Pb solder, reduces the surface tension of pure Sn and improves the wetting properties, reduces the growth of whiskers in Sn, decreases the viscosity of Sn-Pb solder, and prevents the transformation of white tin (β-tin) into gray tin (α-tin) [4, 5]. Notwithstanding their favorable properties, lead-based solder alloys have been largely eliminated from industrial applications owing to the toxic nature of lead and its well-documented adverse impacts on human health and environmental sustainability. On October 11, 2002, members of the European Community (EC) prohibited the use of certain harmful materials or substances in electrical and electronic equipment. It has been decided that four heavy metals (lead, cadmium, mercury and chromium) will no longer be used as of January 1, 2004. In the US, laws have been introduced to eliminate Pb [6]. Environmental and health issues have hindered the widespread use of leaded solder. Legislations such as the Waste in Electrical and Electronic Equipment (WEEE) and the Restriction of the Use of Certain Hazardous Substances (ROHS) have been effective in banning lead in electronic products since August 2005 and July 2006, respectively [7]. Lead-free solders must comply with a range of properties and characteristics to be considered suitable for replacing eutectic Sn-Pb solders for use in electronic assemblies [8]. When substituting conventional Sn–Pb solder alloys, lead-free solders must exhibit performance characteristics comparable to or superior to those of Sn–Pb systems. Accordingly, candidate Pb-free solder alloys should satisfy several essential criteria, including non-toxicity, adequate material availability to support present and future manufacturing demands, and sufficient electrical and thermal conductivity. In addition, these alloys must demonstrate reliable mechanical performance, including strength, toughness, and resistance to fatigue and creep. Compatibility with commonly used surface finishes and terminal metallization (such as Cu, Ni, Ag, Au, Sn, and In) is also essential. Furthermore, acceptable melting behavior and processing temperatures, closely aligned with those of eutectic Sn–Pb solder, are necessary to minimize thermal damage to electronic assemblies, printed circuit boards, and components during soldering operations. Researchers and machinists have begun to identify elements that can replace lead and produce a system that possesses the same properties as Pb-based soldering alloys [9]. There are several elements that can be used to construct a Pb-free solder system with Sn as the base element, such as Ag, Cu, Bi, and Zn [10]. Several types of Sn-based lead-free solder alloys, such as Sn-Zn, Sn-Ag, Sn-Bi, and Sn-Cu, have been developed and applied in the electronic packaging industry [11]. The tin–silver (Sn-Ag) eutectic alloy is considered a suitable choice for substituting– Sn Sn-Pb eutectic solder and has already been used in electronics soldering to a limited extent [12]. Furthermore, this technique is employed in the soldering of stainless-steel components used in food processing applications, where material compatibility and joint reliability are of critical importance. Amid accelerating industrial transformations and the global push toward more sustainable manufacturing technologies, the development of lead-free solder alloys has become a critical priority, especially in high-precision electronic applications [13]. Among the most promising alternatives to conventional Sn–Pb solders are Sn–Ag–Cu alloys, which offer excellent mechanical strength, thermal stability, and environmental compliance [14]. However, enhancing the performance of these alloys requires a thorough investigation of how variations in elemental composition affect their microstructure and physical behavior [15]. This study focuses on evaluating the structural and compositional effects of adding the alloy (x)Ag–(3.5+x)Cu to the near-eutectic (96.5–2x)Sn system. The research involves characterizing the resulting alloys using X-ray diffraction (XRD) to identify the crystalline phases and scanning electron microscopy (SEM) to analyze the microstructural features [16]. The goal is to establish a new alloying model with high efficiency for electronic applications and improve solder joint properties, such as hardness, creep resistance, thermal conductivity, and grain refinement [17]. This study contributes to a deeper understanding of the relationship between chemical composition and structural evolution, offering insights into the long-term reliability of Sn–Ag–Cu-based solder systems [18].

2. MATERIALS AND METHODS

Table 1. Binary and Ternary alloy groups.

Solder alloy WT%	Sn	Ag	Cu	Total
96.3Sn0.1Ag3.6Cu	**96.3%**	**0.1%**	**3.6%**	**100%**
96.1Sn0.2Ag3.7Cu	**96.1%**	**0.2%**	**3.7%**	**100%**
95.9Sn0.3Ag3.8Cu	**95.9%**	**0.3%**	**3.8%**	**100%**
95.7Sn0.4Ag3.9Cu	**95.7%**	**0.4%**	**3.9%**	**100%**
95.5Sn0.5Ag4Cu	**95.5%**	**0.5%**	**4%**	**100%**

High-purity elements of tin (Sn, 99.99%), silver (Ag, 99.99%), and copper (Cu, 99.99%) were selected. Alloys with a nominal composition of (96.5-

2x)Sn–(x)Ag–(3.5+x)Cu were prepared at different concentrations (x = 0.1, 0.2, 0.3, 0.4, and 0.5 wt.%). The elements were weighed precisely using a high-sensitivity electronic balance (FISHER EMD, Model EMD-3100, Serial No: P0108837) with a resolution of 0.1 mg [19]. Five alloy groups were prepared according to the ratios listed in Table 1. The weighed elements were thoroughly mixed to ensure homogeneity and were sealed in Pyrex tubes. Alloying was performed by melting the constituents in an electric furnace at 800 ℃ for 3 h to achieve complete homogenization. After melting, the samples were allowed to cool slowly inside the furnace to room temperature to ensure controlled solidification. The Pyrex tubes were then broken to retrieve the solidified alloys from the tubes. The samples were mechanically polished using silicon carbide papers of different grades and subsequently cleaned with acetone and CH_3COCH_3 solutions. The alloys were then rolled into small sheets for microstructural investigation. To remove the residual stresses induced during sample preparation, the specimens were annealed at (100 $\pm$ 2) ℃ for 6 h and cooled gradually to room temperature at a rate of 1 ℃/min. Structural characterization was performed using X-ray diffraction (XRD) with a Shimadzu EDX-720 diffractometer equipped with Cu–Kα radiation (λ = 1.54056 Å). Data were collected over a 2θ range of 5–75° at 40 kV and 2 mA. Microstructural analysis was conducted using a scanning electron microscope (SEM, JSM-6510LV) in the secondary electron imaging (SEI) mode to enhance the surface topography contrast and resolution. [4]

3. RESULTS AND DISCUSSION

3.1. Structural analysis

Table 2. Represents X-ray diffraction pattern for (JCPDS-ICDD) (PDF# 04-0673) Stander tetragonal phases [20].

No	2θ	d (Å)	hkl	I%
1	30.644	2.915	(200)	100
2	32.018	2.793	(101)	90
3	43.871	2.062	(220)	34
4	44.902	2.017	(211)	74
5	55.330	1.659	(301)	17
6	62.538	1.474	(112)	23
7	63.783	1.458	(400)	13
8	64.576	1.442	(321)	20
9	73.19	1.292	(411)	21

The phase structure and phase content were identified using X-ray diffraction analysis. The data were scanned from 5∘ to 75∘ by (Cuk-α) radiation (λ=1.54056 Å). The source was operated at an accelerating voltage of (40 kV) with a current of 2 mA. Continuous scanning was performed at a constant scanning rate of 0.02/1sec [21]. The path difference for rays reflected from adjacent planes is ($2d\sin\theta$), and constructive interference occurs when the difference in path is an integer, n, of the wavelength [22].

$$n\lambda = 2d\sin\theta \tag{1}$$

There is an inverse relationship between the particle size and broadening of the X-ray curves through the formula given by the Scherrer equation [23]:

$$D = \frac{0.9\lambda}{\beta\cos\theta} \tag{2}$$

where: β is the broadening of the diffraction line, which is the full width at half the maximum intensity (radians) of the peak, D is the particle size, θ is the diffraction angle, and λ is the wavelength of the X-ray. The dislocation density (δ) is defined as the length of dislocation lines per unit volume of the crystal and d is given by [24]:

$$\delta = 1/D^2 \tag{3}$$

The lattice distortion values were calculated using the Williams and Hall formula [25]:

$$\beta_{hkl}\cos\theta = \frac{k\lambda}{D} + 4\varepsilon\sin\theta \tag{4}$$

The slope provides the microstrain ε, and the Y-intercept reveals the crystallite size D, where β is the Full Width at Half Maximum (FWHM) of the peak after instrumental broadening correction (in radians). θ is the Bragg diffraction angle. k = Shape factor, typically $\sim 0.9.\lambda$ =X-ray wavelength. D = Crystallite size. $\varepsilon =$ Lattice micro strain. By plotting $\beta_{hkl}\cos\theta$ versus $4\sin\theta$, a straight line is obtained: The slope provides the micro strain ε. The intercept on the vertical axis gives the crystallite size D [25].

Table 3. XRD pattern for 96.3Sn-0.1Ag-3.6Cu alloy.

No	2θ	d (A^0)	hkl	I%	FWHM	Crystallite size D (nm)	$\delta = \frac{1}{D^2}$ ($\times 10^{-3}$ nm^{-2})
1	31.1	2.873	(200)	100	0.254	51.089	0.383
2	32.48	2.754	(101)	46	0.291	48.919	0.418
3	44.44	2.065	(220)	13.9	0.223	35.753	0.782
4	45.5	1.992	(211)	62	0.295	34.921	0.820
5	56.04	1.639	(301)	11.8	0.289	28.353	1.244
6	63.22	1.469	(112)	5.6	0.215	25.132	1.583
7	64.58	1.442	(400)	7.4	0.277	24.604	1.652
8	65.32	1.427	(321)	31.2	0.292	24.325	1.690
9	73.94	1.281	(411)	9.1	0.38	21.489	2.166
Average						32.732	1.193

Table 4. XRD pattern for 96.1Sn-0.2Ag-3.7Cu alloy.

No	2θ	d (A^0)	hkl	I%	FWHM	Crystallite size D (nm)	$\delta = \frac{1}{D^2}$ $\times 10^{-3}$ nm^{-2})
1	31.47	2.841	(200)	30.2	0.305	50.492	0.392
2	32.79	2.729	(101)	58.4	0.562	48.459	0.426
3	45.43	1.995	(211)	100	0.519	34.974	0.818
4	56.14	1.637	(301)	33.2	0.309	28.304	1.248
5	63.20	1.470	(400)	13.5	0.641	25.143	1.582
6	65.34	1.427	(321)	82.3	0.419	24.319	1.691
7	74.14	1.278	(411)	20.7	0.468	21.431	2.177
Average						33.303	1.191

The results indicate that all synthesized alloys exhibit a near-eutectic microstructural classification, which

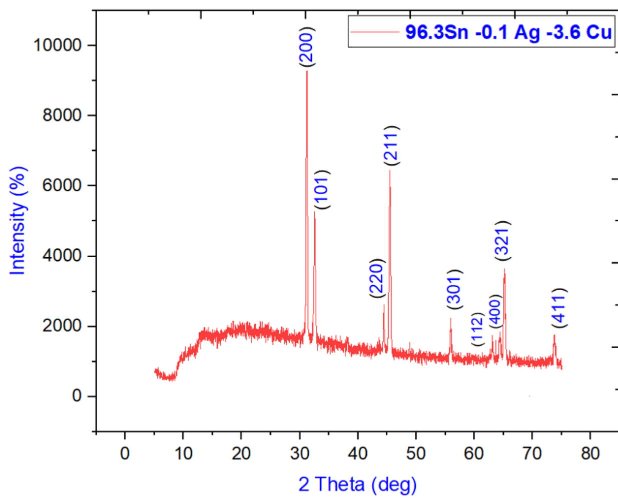

Figure 1. XRD pattern for 96.3Sn -0.1 Ag -3.6 Cu alloy.

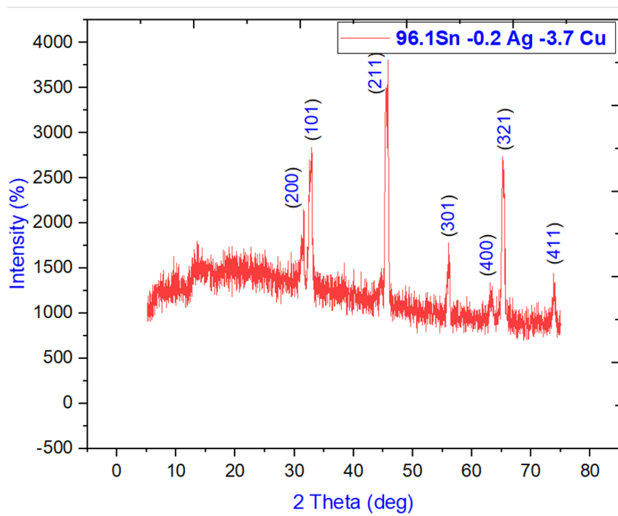

Figure 2. XRD pattern for 96.1 Sn -0.2 Ag -3.7 Cu alloy.

Table 5. XRD pattern for 95.9Sn-0.3Ag-3.8Cu alloy.

No	2δ	d (A^0)	hkl	I%	FWHM	Crystallite size D (nm)	$\delta = \frac{1}{D^2}$ ($\times 10^{-3}$ nm^{-2})
1	30.6	2.919	(200)	100	0.229	51.924	0.371
2	31.96	2.798	(101)	30	0.259	49.716	0.405
3	44.96	2.015	(211)	81.8	0.31	35.339	0.801
4	55.5	1.645	(301)	11.2	0.275	28.628	1.220
5	64.82	1.437	(321)	44.7	0.351	24.512	1.664
6	73.46	1.288	(411)	15.3	0.291	21.629	2.138
Average						35.292	1.099

Table 6. XRD pattern for 95.7Sn-0.4Ag-3.9Cu alloy.

No	2θ	d (A^0)	hkl	I%	FWHM	Crystallite size D (nm)	$\delta = \frac{1}{D^2}$ ($\times 10^{-3}$ nm^{-2})
1	30.96	2.89	(200)	42.9	0.396	51.321	0.379
2	32.34	2.77	(101)	42.1	0.317	49.131	0.414
3	44.32	2.04	(220)	12.5	0.205	35.852	0.778
4	45.28	2.00	(211)	100	0.276	35.090	0.812
5	55.80	1.65	(301)	14.2	0.307	28.494	1.233
6	63.04	1.47	(400)	15.5	0.237	25.204	1.574
7	65.12	1.43	(321)	34.7	0.233	24.399	1.679
8	73.78	1.28	(411)	14.3	0.23	21.536	2.156
Average						33.876	1.128

is characteristic of (96.5-2x)Sn-(x)Ag-(3.5+x)Cu with (x=0.1, 0.2,0.3,0.4 and 0.5 wt. %) systems. X-ray diffrac-

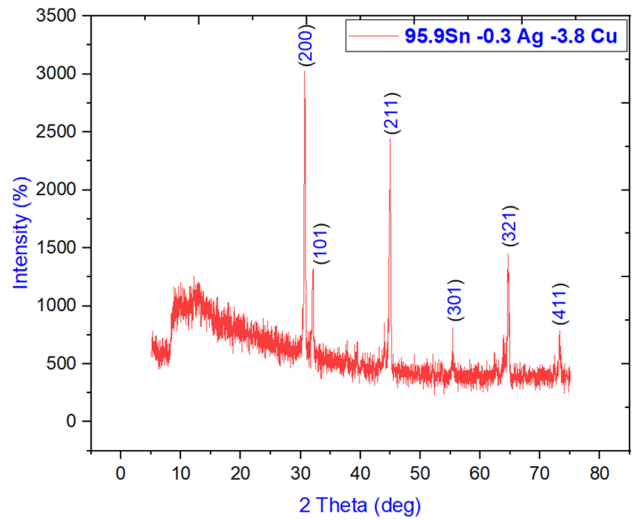

Figure 3. XRD pattern for 95.9 Sn -0.3 Ag -3.8 Cu alloy.

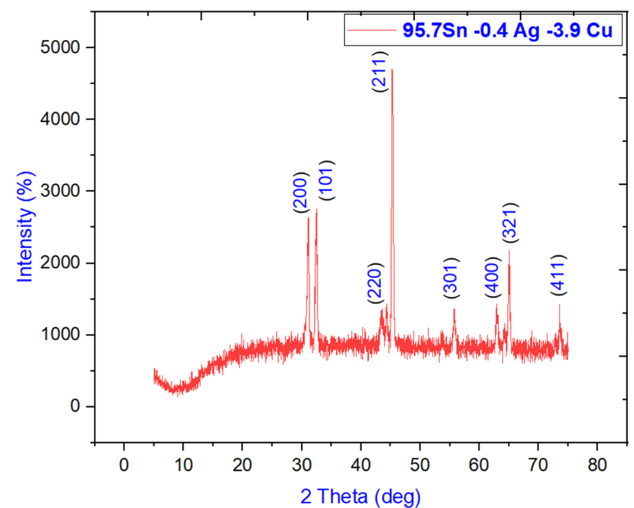

Figure 4. XRD pattern for 95.7 Sn -0.4 Ag -3.9 Cu alloy.

Table 7. XRD pattern for 95.5Sn-0.5Ag-4Cu alloy.

No	2θ	d (A0)	hkl	I%	FWHM	Crystallite size D (nm)	$\delta = \frac{1}{D^2}$ ($\times 10^{-3}$ nm^{-2})
1	30.98	2.884	(200)	65.4	0.175	51.288	0.380
2	32.36	2.764	(101)	100	0.196	48.949	0.417
3	44.30	2.043	(220)	7.5	0.209	35.865	0.777
4	45.34	1.999	(211)	84	0.213	35.044	0.814
5	55.84	1.645	(301)	14.5	0.205	28.453	1.235
6	63.08	1.479	(400)	13.7	0.212	25.188	1.576
7	65.16	1.431	(321)	24.3	0.215	24.384	1.682
8	73.8	1.283	(411)	9.1	0.192	21.529	2.157
Average						33.838	1.129

tion (XRD) analysis confirmed that the dominant phase in all samples is $\beta - Sn$, crystallizing in a tetragonal single-phase structure [Yakymovych & Shtablavyi, 2023] [26]. The diffraction patterns, illustrated in Figures (1–5), reveal closely spaced peaks in the 2θ range, accompanied by noticeable shifts in peak positions and variations in intensity and full width at half maximum (FWHM). These observations suggest phase overlap, atomic migration within the crystal lattice, and redistribution phenomena, ultimately leading to grain refinement and modifications in interplanar spacing [27, 28]. From the diffraction pro-

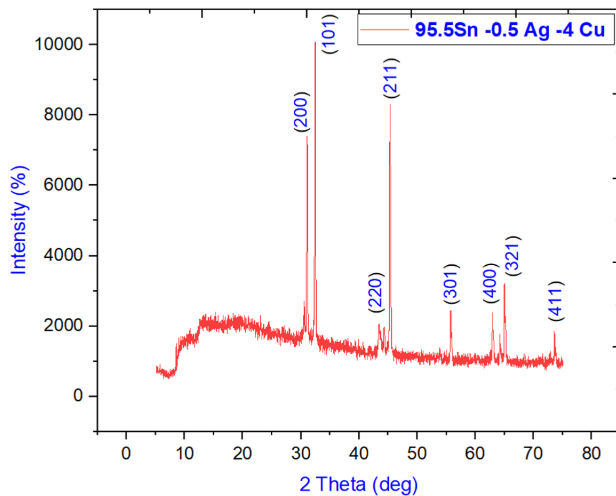

Figure 5. XRD pattern for 95.5 Sn -0.5 Ag - 4 Cu alloy.

files, two key features can be highlighted: Sharp peaks indicate well-ordered, stable phases and the presence of large crystallites. High-intensity peaks are predominantly associated with Sn-rich regions [29]. Yakymovych and Shtablavyi (2023) reported enhanced crystallinity and phase redistribution in Sn–3.0Ag–0.5Cu alloys reinforced with nanoscale Ni, which is consistent with the peak shifts and intensity variations observed in the present study [26]. XRD analysis of the (96.5-2x)Sn-(x)Ag-(3.5+x)Cu with (x=0.1, 0.2,0.3,0.4 and 0.5 wt. %) system revealed the predominance of the β-Sn phase, with no detectable peaks corresponding to intermetallic compounds such as Ag_3Sn and Cu_6Sn_5. This observation is consistent with previous reports, where Yakymovych and Shtablavyi (2023) demonstrated that nanoscale Ni reinforcements in Sn–3.0Ag–0.5Cu alloys enhance crystallinity and induce phase redistribution, leading to the suppression or weakening of intermetallic peak intensities. Similarly, Machajdíková et al. (2024) investigated the phase composition of Sn–3.0Ag–0.5Cu alloys with Ni additions and confirmed that the β-Sn phase dominates the diffraction profiles, while intermetallic compounds remain either undetectable or present in negligible amounts. These findings collectively support the interpretation that the β-Sn phase is the primary crystalline constituent under the studied conditions, with intermetallic phases being below the detection threshold of XRD [26, 30]. The absence of these peaks can be explained by several factors: The relatively low additions of Ag and Cu (x = 0.1–0.5 wt. %) may fall below the detection limit of XRD [31]. The characteristic peaks of intermetallic compounds may be weak or overlapped [28]. This interpretation aligns with previous studies on nanostructured Sn–Ag–Cu alloys, which reported that intermetallic phases may not be clearly detected at low concentrations or when fine grain fragmentation occurs [31]. Therefore, the absence of diffraction peaks does not necessarily imply the absence of intermetallic compounds but may instead reflect detection limitations or spectral overlap. Additionally, XRD analysis confirmed that all samples exhibit a single-phase structure with a body-centered tetragonal lattice. Examination of the internal structure through XRD patterns revealed that in sample 1, the (200) plane is the dominant reflection with 100% intensity, containing different atoms of the compound. In sample 2, due to atomic redistribution, the dominant plane shifted to (211). Likewise, in sample 5, the main plane became (101). These changes in dominant planes indicate that the atoms were redistributed within the lattice to form a single-phase compound without the formation of intermetallic compounds (IMCs) [32].

3.2. Crystalline size, and dislocation density:

The crystalline size (D) values of (96.5-2x)Sn-(x)Ag-(3.5+x)Cu with (x=0.1, 0.2,0.3,0.4 and 0.5 wt.%) %) solder alloys were calculated according to the Scherrer formula (2) and are shown in Table 8.

Table 8. Crystalline size(D)and Dislocation density (96.5-2x) Sn(x) Ag (3.5+x) Cu alloys

Samples	Crystalline size(D) (nm)	Dislocation density ($\times 10^{-3}$ nm^{-2})
96.3Sn0.1Ag3.6Cu	32.732	1.193
96.1Sn0.2Ag3.7Cu	33.303	1.191
95.9Sn0.3Ag3.8Cu	35.292	1.099
95.7Sn0.4Ag3.9Cu	33.876	1.128
95.5Sn0.5Ag4Cu	33.838	1.129

Table 8 presents the calculated average particle crystalline size (D) values of the $(96.5-2x)Sn-(x)Ag-(3.5+x)Cu$ solder alloys ($x = 0.1-0.5wt.$ %) were calculated using the Scherrer equation, as shown in Table 8. The data revealed that the average crystallite size increased with Ag and Cu additions up to $x = 0.3$, followed by a slight decrease at higher concentrations ($x = 0.4$ and 0.5). This trend reflects the influence of the alloying elements on the solidification dynamics and microstructural evolution [33]. The observed grain refinement with increasing x can be explained by a specific metallurgical mechanism. During cooling and solidification, Ag and Cu atoms act as barriers to grain growth by segregating at the grain boundaries and impeding the advance of the solidification front [34]. Their atomic radii differ from that of Sn, introducing lattice distortions that hinder atomic diffusion and restrict the coalescence of larger grains. This results in enhanced nucleation rates, microstructural fragmentation, and ultimately the formation of finer grains. Furthermore, the incorporation of Ag and Cu increases the internal strain and dislocation density, which contributes to defect accumulation and promotes structural subdivision [35]. This is also consistent with recent studies on low-Ag SAC alloys, where structural redistribution and localized segregation have been shown to im-

©2026 JAST

prove homogeneity and reduce grain size [36]. Thus, the combined effects of solute segregation, lattice distortion, and defect generation explain the observed refinement in crystallite size at higher Ag/Cu concentrations, reinforcing the role of these alloying elements in tailoring the microstructure of Sn–Ag–Cu solder systems [37].

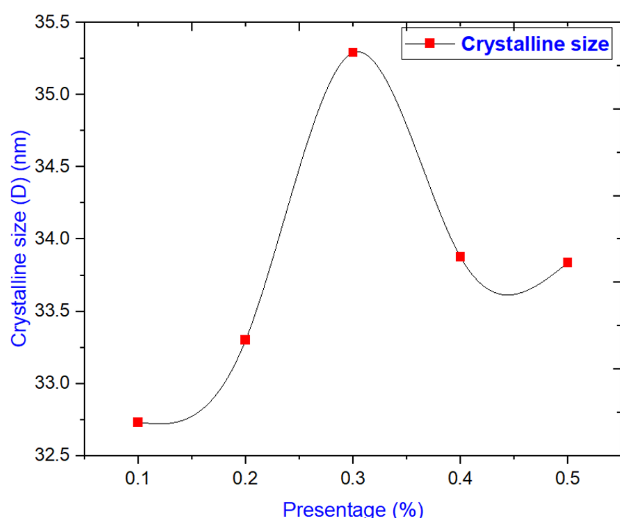

Figure 6. The particle size values of (96.5-2x) Sn(x)Ag(3.5+x)Cu alloy.

The dislocation density (δ) of the (96.5–2x)Sn –(x)Ag – (3.5+x)Cu alloys (x = 0.1, 0.2, 0.3, 0.4, 0.5 wt. %) was quantitatively evaluated using the relation:

$$\delta = 1/D^2 \quad (5)$$

where D represents the average crystallite size determined from X-ray diffraction (XRD) peak broadening, applying either the Scherrer equation or the Williamson–Hall method [38]. The calculated values are summarized in Table 8, and the variation with Ag and Cu content is shown in Figure 7. The results reveal that changes in crystallite size directly influence dislocation density: smaller crystallites correspond to higher δ values due to the increased density of grain boundaries and interfaces that obstruct dislocation motion [39]. Initially, δ decreases as x increases from 0.1 to 0.3, coinciding with an increase in crystallite size from 32.7 nm to 35.3 nm. Larger crystallites reduce the number of grain boundaries per unit volume, thereby lowering dislocation density (from 1.193 to 1.099 nm^{-2}). At higher alloying levels (x = 0.4 and 0.5), crystallite size decreases again to $\sim$33.8 nm, which increases the density of grain boundaries and promotes dislocation accumulation, raising δ to 1.128–1.129 nm^{-2}. This non-monotonic trend reflects the competing effects of crystallite growth and lattice distortion. While larger crystallites reduce defect density, the atomic size mismatch between Sn, Ag, and Cu introduces localized strain fields that hinder dislocation mobility and stimulate the generation of additional dislocations [40]. The combined addition of Ag and Cu produces a stronger refinement effect than Cu alone. This is attributed to differences in atomic radii and solubility limits of Ag and Cu in the Sn matrix. When both elements are introduced simultaneously, overlapping strain fields are generated at multiple lattice sites due to atomic size mismatch. These intensified distortions act as effective barriers to dislocation glide and climb, promoting dislocation accumulation and increasing overall defect density [41]. This synergistic interaction enhances the Hall–Petch strengthening mechanism: the higher density of grain boundaries and strain fields restricts dislocation mobility more effectively than in binary Sn–Cu alloys. Ag contributes to structural redistribution and improved homogeneity, while Cu promotes the formation of semi-coherent interfaces with the Sn lattice. Together, they provide dual strengthening pathways—grain boundary strengthening and solid solution strengthening—leading to improved mechanical hardness and stability [37]. The results confirm that the co-doping of silver (Ag) and copper (Cu) in Sn–Ag–Cu alloys produce a synergistic effect that surpasses the strengthening achieved in binary Sn–Cu systems. This interaction enhances the Hall–Petch mechanism by increasing grain boundary density and generating strain fields arising from atomic size mismatch between alloying elements. Ko et al. (2022) demonstrated through atomistic simulations that the simultaneous introduction of Ag and Cu intensifies lattice distortions, which act as effective barriers to dislocation glide and climb, thereby increasing dislocation density and improving mechanical stability. Similarly, El-Taher et al. (2025) reported that variations in atomic radii and solubility limits among alloying elements in the Sn matrix promote dual strengthening pathways—grain boundary strengthening and solid solution strengthening. Ag contributes to structural redistribution and improved homogeneity, while Cu facilitates the formation of semi-coherent interfaces with the Sn lattice, collectively enhancing hardness and stability. In addition, Sun et al. (2024) provided experimental evidence showing that Sn–Ag–Cu alloys exhibit the formation of sub grains and intensified lattice distortions compared to Sn–Cu alloys, further restricting dislocation mobility and amplifying Hall–Petch strengthening [34]. This experimental validation complements atomistic simulations and confirms that the balance between crystallite size refinement and lattice distortions governs dislocation behavior and mechanical performance. Thus, the synergy between Ag and Cu additions provides a robust dual strengthening mechanism, aligning both theoretical and experimental findings with the microstructural evolution observed in Figures 6 and 7 and Table 8.

©2026 JAST

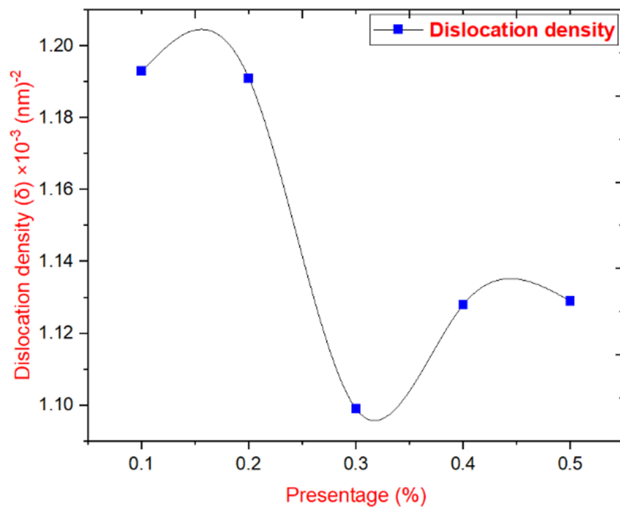

Figure 7. The variation in dislocation density values of (96.5-2x)Sn(x)Ag(3.5+x)Cu alloy.

3.3. The X-ray density (D_x) and bulk density (D_b)

In the (96.5-2x) Sn-(x) Ag-(3.5+x) Cu alloy, with x = 0.1, 0.2, 0.3, 0.4, and 0.5 wt%,the X-ray density (Dx) consistently appears higher than the bulk density (Db) because Dx is derived from the ideal crystallographic unit cell parameters, whereas Db reflects the actual measured mass-to-volume ratio of the alloy, which is reduced by porosity, microvoids, and lattice defects. Recent studies have confirmed that this divergence is a reliable indicator of microstructural imperfections in lead-free solders [42]. X-ray Density (Dx), The parameter Dx, representing the idealized atomic packing of a crystal lattice, is calculated from crystallographic data as follows Eq. (6):

$$D_x = \frac{ZM}{VN_A} \tag{6}$$

Here, Z is the number of atoms per unit cell, M is the molar mass, N_a is Avogadro's number (6.022 × 10^{23} mol^{-1}), and V is the unit cell volume obtained from the lattice parameters. This calculation assumes a perfect lattice, neglecting defects and porosity [21]. Bulk Density (Db), Definition: Experimentally measured as

$$D_b = \frac{M}{V} \tag{7}$$

Where M is the sample mass and V is the macroscopic volume [43]. Porosity and voids are formed during solidification. Microcracks induced by thermal cycling. Grain boundary irregularities [44]. The consistent observation that the X-ray density (Dx) exceeds the bulk density (Db) in (96.5–2x) Sn–(x) Ag–(3.5+x) Cu alloys (x = 0.1–0.5 wt. %) provides a reliable diagnostic tool for microstructural imperfections. As the Ag and Cu contents increased, the mass of the alloy increased, leading to a gradual increase in Db. However, Dx does not scale proportionally because of lattice interference effects and irregular atomic packing. This divergence highlights the role of porosity, microvoids, and lattice defects in reducing the effective density [45]. Cullity and Stock (2001) established the theoretical basis of X-ray density, showing that Dx is derived from ideal crystallographic unit cell parameters and assumes perfect atomic packing [21]. In contrast, Varanasi and Pal (2021) emphasized that Db is experimentally measured as the mass-to-volume ratio, inherently reflecting structural imperfections such as porosity and voids [43]. Complementing these findings, Wang et al. (2019) demonstrated that microstructural defects, including voids and irregular grain boundaries, significantly influence solder joint reliability, thereby explaining the persistent mismatch between Dx and Db. Together, these references confirm that the Dx–Db divergence is not merely a measurement artifact but a distinctive hallmark of microstructural imperfections in lead-free solder alloys. This makes the comparison between the theoretical and experimental densities a valuable tool for evaluating the quality and reliability of alloys in electronic packaging applications [46]. The axial ratio variation (c/a) is presented in Table 4. The maximum value of the axial ratio c/a = 0.549 nm was observed at x=0.4wt. % of Ag [32]. The plane-spacing equation for this system involves two unknown parameters, a and c [47].

$$\frac{1}{d^2} = \frac{h^2+k^2}{a^2} + \frac{l^2}{c^2} \tag{8}$$

where d is the inter-planar spacing or distance between layers, and h, k, and l are Miller indices.

This may be rewritten in the form:

$$\frac{1}{d^2} = \frac{1}{a^2}\left[\left(h^2+k^2\right) + \frac{l^2}{\left(\frac{c}{a}\right)^2}\right] \tag{9}$$

The best method to investigate the change in the matrix structure is to evaluate the c/a ratio and the volume of the tetragonal unit cell [48], where the volume of the tetragonal unit cell is

$$V = a^2.c \tag{10}$$

Table 9. The ratio between (c/a).

Samples	Cu addition %	Ag addition %	Sn addition %	a (nm)	c (nm)	(C/a)
96.3Sn0.1Ag3.6Cu	3.6	0.1	96.3	0.575	0.3138	0.545
96.1Sn0.2Ag3.7Cu	3.7	0.2	96.1	0.578	0.3139	0.543
95.9Sn0.3Ag3.8Cu	3.8	0.3	95.9	0.584	0.3167	0.542
95.7Sn0.4Ag3.9Cu	3.9	0.4	95.7	0.577	0.3167	0.549
95.5Sn0.5Ag4Cu	4	0.5	95.5	0.579	0.3147	0.544

3.4. Scanning Electron Microscopy (SEM) Analyses

The front of the detector contained a screen biased at (200 V). Since most of the secondary electrons have en-

Table 10. The X-ray density (Dx) and bulk density (Db).

Samples	Dx (gm/cm^3)	Db (gm/cm^3)
96.3Sn0.1Ag3.6Cu	7.482	7.189
96.1Sn0.2Ag3.7Cu	7.395	7.172
95.9Sn0.3Ag3.8Cu	7.169	7.123
95.7Sn0.4Ag3.9Cu	7.333	7.181
95.5Sn0.5Ag4Cu	7.342	7.114

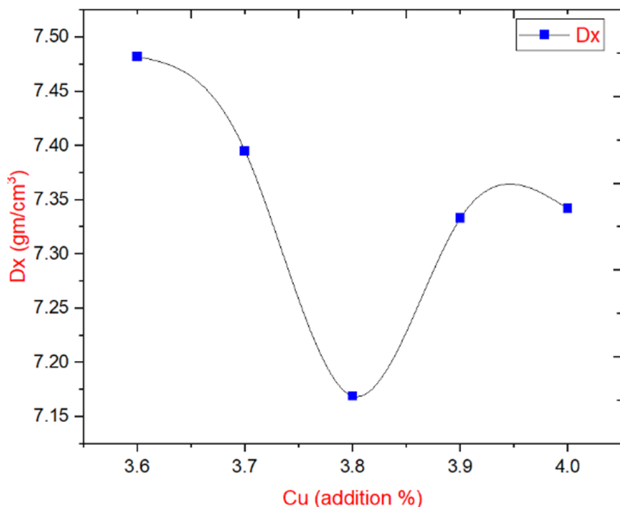

Figure 8. The X-ray density (Dx) of (96.5-2x) Sn(x) Ag(3.5+x) Cu with (Cu) addition (%).

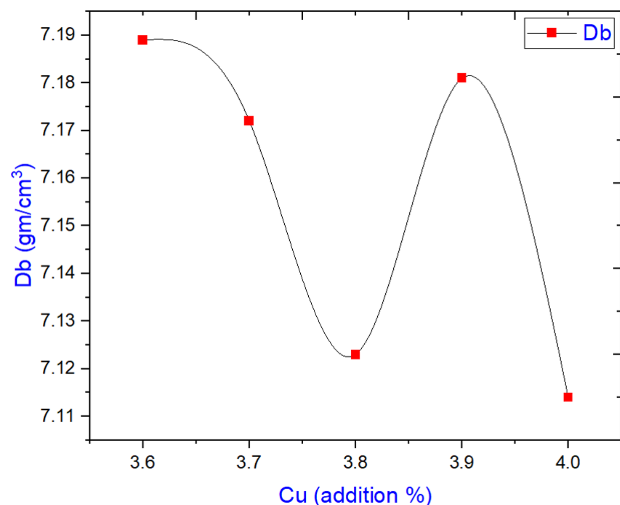

Figure 9. The bulk density (Db) of (96.5-2x)Sn (x)Ag (3.5+x)Cu with (Cu) addition (%).

ergies only of the order of (3 to 5 eV), these low-energy electrons tend to be easily drawn into the detector by its (200 V) bias [49]. In the part of the specimen surface used to form the image, that is the raster, the electron beam is swept along a straight line over the entire width of the raster, as indicated. In standard scanning electron microscopy (SEM) imaging, the specimen is scanned using a raster pattern composed of approximately 1000 scan lines to generate a micrograph with dimensions of 10 × 10 cm [49, 50]. The scanning cycle was repeated at a frame rate of 30 frames per second (fps)

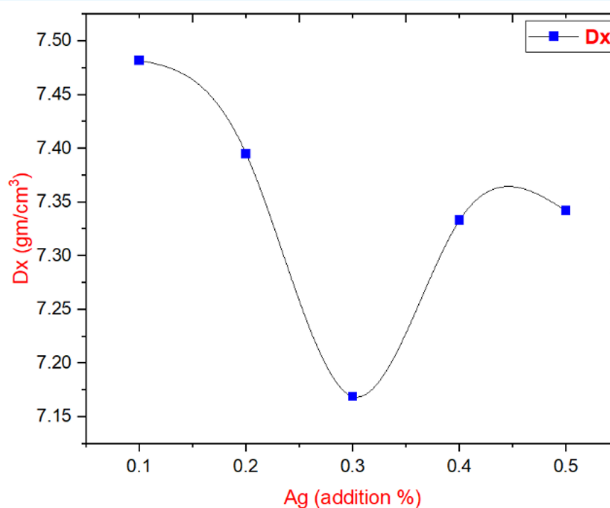

Figure 10. The X-ray density (Dx) of (96.5-2x) Sn(x) Ag(3.5+x) Cu with (Ag) addition (%).

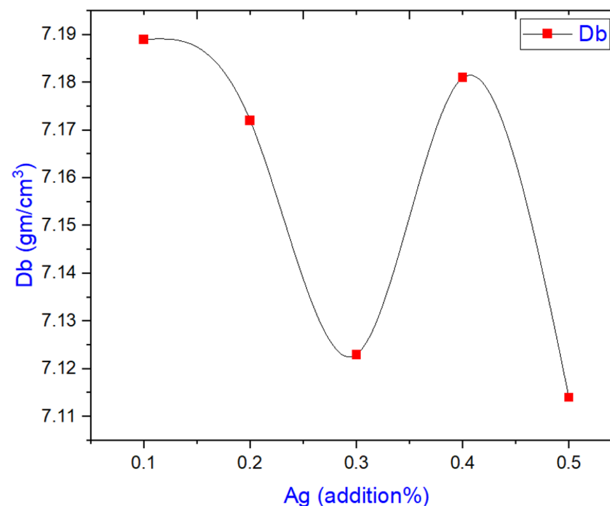

Figure 11. The bulk density (Db) of (96.5-2x)Sn (x)Ag (3.5+x)Cu with (Ag) addition (%).

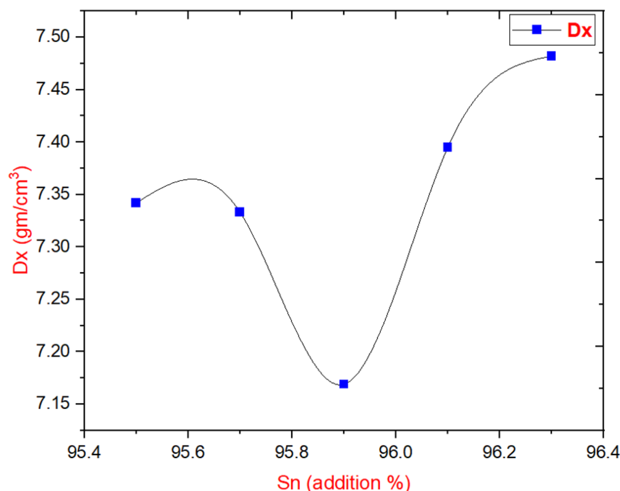

Figure 12. The X-ray density (Dx) of (96.5-2x) Sn(x) Ag(3.5+x) Cu with (Sn) addition (%).

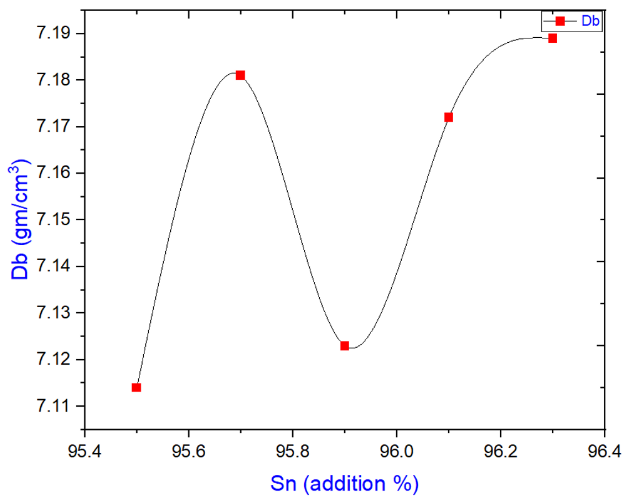

Figure 13. The bulk density (Db) of (96.5-2x)Sn (x)Ag (3.5+x)Cu with (Sn) addition (%).

to ensure real-time image acquisition. The resulting image was captured and displayed using a cathode ray tube (CRT) equipped with a short-persistence phosphor screen, which minimized image lag and enhanced temporal resolution, thereby preserving the clarity and fidelity of rapidly updated frames [49].

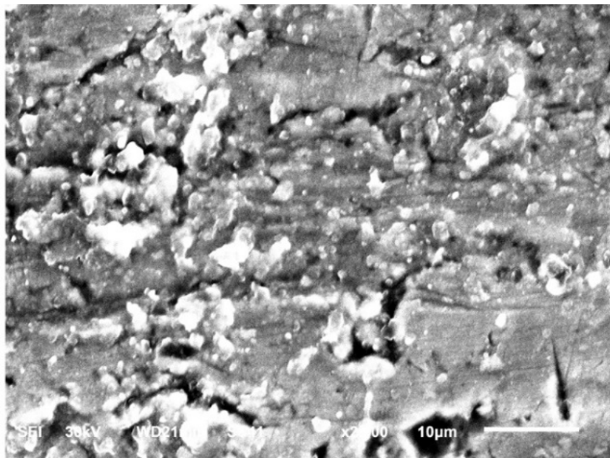

Figure 14. SEM images of 96.3 Sn 0.1 Ag 3.6 Cu alloy.

SEM micrographs obtained at ×2000 magnification under an accelerating voltage of 30 kV revealed a rough and irregular surface morphology of the (96.5-2x)Sn–(x)Ag–(3.5+x)Cu with (x = 0.1, 0.2, 0.3, 0.4, and 0.5 wt. %) alloy. The surface exhibited fine grains of varying sizes, shallow pits, and localized cracks, reflecting heterogeneous solidification and the influence of rapid cooling during alloy processing [51]. Dark Gray Regions (Background): Represent the β-Sn matrix phase, forming the primary structural framework of the alloy. These areas appear relatively smooth, consistent with the bulk tin phase [52]. Light Gray Features: Correspond to protrusions and irregular grains. Their brightness in SEL mode is linked to surface topography, highlighting uneven solidification fronts [53]. Bright White Spots: Indicate sharp edges or grain boundaries where secondary electron emission is enhanced due to local surface geometry [34]. These regions often coincide with microstructural discontinuities. Black Areas: Denote micro-voids or shrinkage porosity formed during rapid solidification. Their absence of secondary electron signal confirms localized depressions or cavities. The absence of large pores or deep

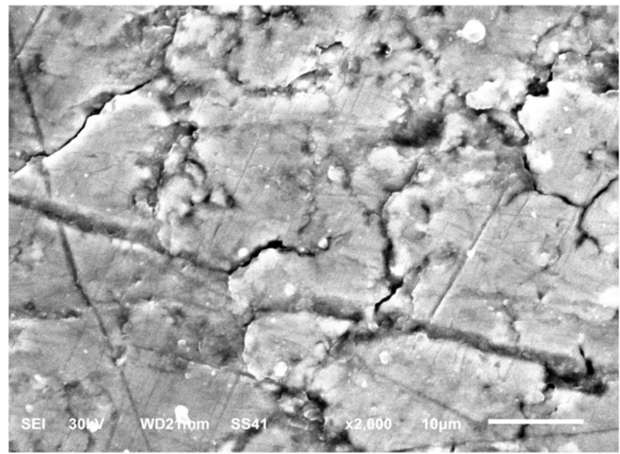

Figure 15. SEM images of 96.1 Sn 0.2 Ag 3.7 Cu alloy.

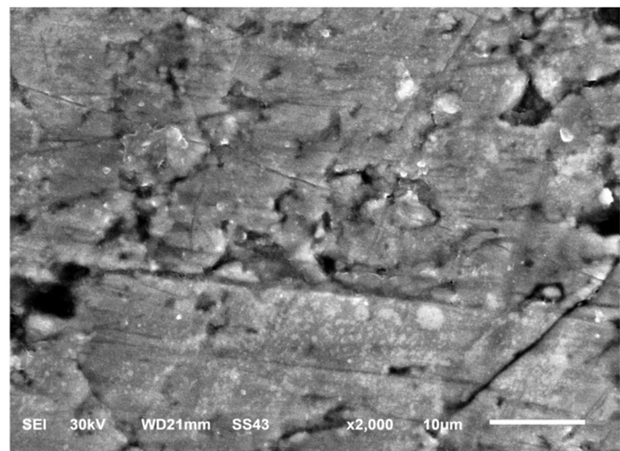

Figure 16. SEM images of 95.9 Sn 0.3 Ag 3.8 Cu alloy.

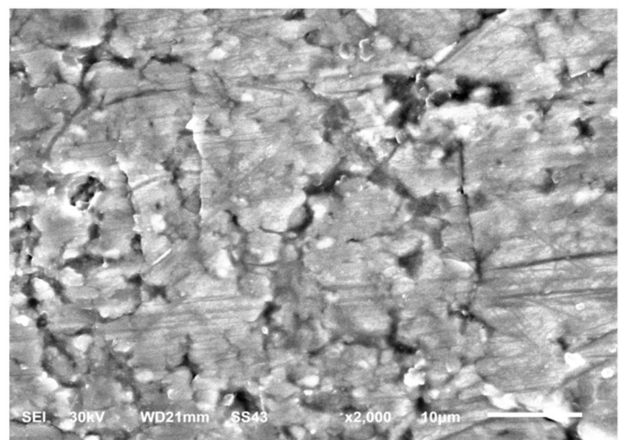

Figure 17. SEM images of 95.7 Sn 0.4 Ag 3.9 Cu alloy.

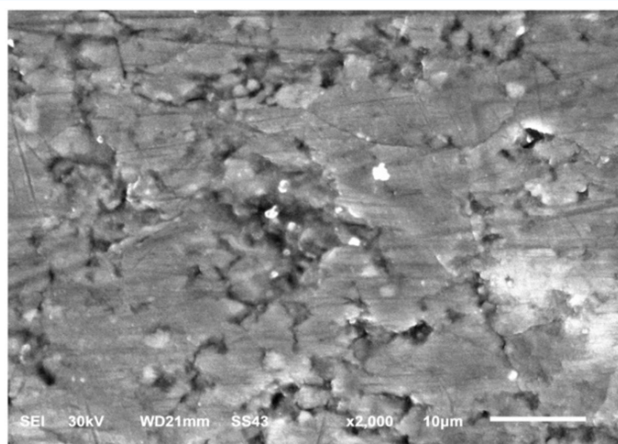

Figure 18. SEM images of 95.5 Sn 0.5 Ag 4 Cu alloy.

cracks suggests high solidification quality and mechanical reliability, which is critical for solder joint performance in electronics. However, the observed grain irregularity and micro-porosity highlight the influence of cooling rate on microstructural refinement [54]. Scanning electron microscopy (SEM) revealed compositional variations at the microscale, where regions enriched with tin (Sn), silver (Ag), and copper (Cu) were distributed within the matrix. These features should not be interpreted as distinct secondary phases, but rather as local compositional heterogeneities within the β-Sn framework. The consistency between X-ray diffraction (XRD) evidence indicating phase stability and SEM observations of elemental segregation demonstrates that the alloys retain structural homogeneity at the crystallographic scale, while exhibiting microstructural partitioning at the sub-grain level [54, 55].

4. CONCLUSION

This study successfully developed a series of ternary solder alloys with the nominal composition (96.5-2x)Sn–(x)Ag–(3.5+x)Cu, where x = 0.1–0.5, aimed at optimizing structural and microstructural properties for lead-free electronic applications. X-ray diffraction (XRD) analysis confirmed the absence of any additional peaks, indicating the high purity of the materials and the successful incorporation of Sn–Ag–Cu into the lattice without forming secondary phases. This demonstrates that the crystal structure of the samples is stable in a single-phase, body-centered tetragonal form, with a three fold axis and a high degree of symmetry. Subtle peak shifts and improved grain definition at higher Ag and Cu concentrations further indicated lattice strain and enhanced crystallinity. At the same time, scanning electron microscopy (SEM) revealed compositional variations at the microscale, with Sn-, Ag-, and Cu-enriched regions distributed within the matrix. These features should not be interpreted as distinct secondary phases but rather as local compositional heterogeneities within the β-Sn framework. The coexistence of XRD evidence for phase stability and SEM observations of elemental segregation suggests that the alloys maintain structural homogeneity at the crystallographic scale, while exhibiting microstructural partitioning at the sub-grain level. Additionally, the consistent finding that the X-ray density (Dx) exceeded the bulk density (Db) for all alloys highlights the presence of microstructural imperfections such as porosity and lattice defects. This divergence serves as a useful diagnostic indicator of alloy quality and reliability in electronic packaging. Overall, the results demonstrate that controlled additions of Ag and Cu reinforce phase stability, improve crystallinity, and enhance microstructural integrity, positioning the (96.5-2x)Sn–(x)Ag–(3.5+x)Cu system, where x = 0.1–0.5, as a promising candidate for high-performance, lead-free solder materials in next-generation microelectronics.

REFERENCES

[1] O. Abdelhadi, “Size effects in tin-based lead-free solder joints: Kinetics of bond formation and mechanical characteristics,” Ph.D. dissertation, University of Alabama, 2013.

[2] M. Abtew and G. Selvaduray, “Lead-free solders in microelectronics,” *Mater. Sci. Eng. R: Reports*, vol. 27, no. 5–6, pp. 95–141, 2000.

[3] K. Sinha et al., “Effect of printed circuit board design parameters on solder joint reliability for memory packages,” in *Proceedings of the IEEE 24th Electronics Packaging Technology Conference (EPTC)*, 2022.

[4] Z. Miric, A. Miric, and A. Grusd, “Lead-free alloys,” *Solder. & Surf. Mt. Technol.*, vol. 10, no. 1, pp. 19–25, 1998.

[5] O. R. Adetunji et al., “Tensile, hardness and microstructural properties of sn–pb solder alloys,” *Mater. Today: Proc.*, vol. 44, pp. 321–325, 2021.

[6] K. Biedenkopf, “Hazardous substances in electronics: The effects of european union risk regulation on china,” *Eur. J. Risk Regul.*, vol. 3, no. 4, pp. 477–487, 2012.

[7] P. Rawana, “Restriction of hazardous substances in electrical and electronic equipment (rohs) policy in the uk,” Tech. Rep., 2010.

[8] H. Ma and J. C. Suhling, “A review of mechanical properties of lead-free solders for electronic packaging,” *J. Mater. Sci.*, vol. 44, no. 5, pp. 1141–1158, 2009.

[9] S. Li et al., “Corrosion behavior of sn-based lead-free solder alloys: A review,” *J. Mater. Sci. Mater. Electron.*, vol. 31, no. 12, pp. 9076–9090, 2020.

[10] C. M. L. Wu et al., “Properties of lead-free solder alloys with rare earth element additions,” *Mater. Sci. Eng. R: Reports*, vol. 44, no. 1, pp. 1–44, 2004.

[11] N. Kumar and A. Maurya, “Development of lead-free solder for electronic components based on thermal analysis,” *Mater. Today: Proc.*, vol. 62, pp. 2163–2167, 2022.

[12] Y. Cui et al., “Nucleation and growth of ag_3sn in sn–ag and sn–ag–cu solder alloys,” *Acta Materialia*, vol. 249, p. 118 831, 2023.

[13] K. Serizawa, M. Okamoto, and H. Shimokawa, “Overview of ims project: Next generation environment-friendly soldering technology,” *J. Jpn. Inst. Electron. Packag.*, vol. 5, no. 3, pp. 207–211, 2002.

[14] B. Li et al., “The effect of indium microalloying on lead-free solders: A review,” *Mater. Sci. Semicond. Process.*, vol. 185, p. 108 956, 2025.

[15] M. Aamir et al., “A review of microstructure and properties of tin–silver–copper lead-free solder series for electronic applications,” *Solder. & Surf. Mt. Technol.*, vol. 32, no. 2, pp. 115–126, 2020.

[16] M. Reid et al., “Effect of ag content on the microstructure of sn–ag–cu based solder alloys,” *Solder. & Surf. Mt. Technol.*, vol. 20, no. 4, pp. 3–8, 2008.

[17] M. Tamizi et al., “Cobalt–graphene nanosheets enhanced sn–0.3ag–0.7cu composite solder,” *Mater. Sci. Eng. A*, vol. 894, p. 146 199, 2024.

[18] M. Oh, N. Tokunaga, and E. Kobayashi, “Reactive diffusion at the interface between cu and sn–ag alloys,” *J. Mater. Res. Technol.*, vol. 30, pp. 9531–9541, 2024.

[19] M. O. Alam, Y. C. Chan, and K.-N. Tu, “Effect of 0.5 wt.% cu addition in sn–3.5ag solder,” *J. Appl. Phys.*, vol. 94, no. 12, pp. 7904–7909, 2003.

[20] JCPDS–ICDD, *Powder diffraction file, card no. 04-0673*.

[21] B. D. Cullity and S. R. Stock, *Elements of X-ray Diffraction*, 3rd ed. Prentice-Hall, 2001.

[22] C. J. Humphreys, “The significance of bragg’s law in electron diffraction,” *Philos. Mag.*, vol. 93, no. 1, pp. 45–50, 2013.

[23] A. Monshi, M. R. Foroughi, and M. R. Monshi, “Modified scherrer equation for nanocrystallite size estimation,” *World J. Nano Sci. Eng.*, vol. 2, no. 3, pp. 154–160, 2012.

[24] I. W. Sutapa et al., “Dislocation and lattice strain of mgo nanoparticles,” *J. Physics: Conf. Ser.*, vol. 979, p. 012 021, 2018.

[25] V. D. Mote, Y. P. Purushotham, and B. N. Dole, “Williamson–hall analysis of lattice strain in zno nanoparticles,” *J. Theor. Appl. Phys.*, vol. 6, no. 1, p. 6, 2012.

[26] A. Yakymovych and I. Shtablavyi, “Effect of nanosized ni reinforcements on sn–3.0ag–0.5cu alloy,” *Metals*, vol. 13, no. 6, p. 1093, 2023.

[27] V. S. S. Kumar and K. V. Rao, “X-ray peak broadening analysis and optical studies of zno nanoparticles,” *J. Nano- Electron. Phys.*, vol. 5, no. 2, p. 02 026, 2013.

[28] A. H. A. Albhadi, “Study of the structural and mechanical properties of (sn-ag–18in)% alloys solders with x=1, 2, 3, 4 and 5,” Ph.D. dissertation, Sana’a University, 2022.

[29] A. A. M. Othman, A. H. Al-Hammadi, and S. H. Khoreem, “Fabrication and study of the effect of mn-substituted ba-zn nanoferrites on the enrichment of structural properties,” *Sana’a Univ. J. Appl. Sci. Technol.*, vol. 1, no. 2, 2023.

[30] T. Machajdíková et al., “Impact of nickel addition on the phase composition and properties of sn–ag–cu solder alloys,” *J. Physics: Conf. Ser.*, vol. 2931, p. 012 001, 2024.

[31] J.-I. Lee et al., “Fabrication and characterization of sn-based solder alloys,” *J. Korean Cryst. Growth Cryst. Technol.*, vol. 28, no. 3, pp. 130–134, 2018.

[32] A. Leineweber, “The cu–sn system: A comprehensive review,” *J. Phase Equilibria Diffusion*, vol. 44, no. 3, pp. 343–393, 2023.

[33] H. Bai et al., “Influence of ag content on the formation and growth of intermetallic compounds in sn–ag–cu solder,” *J. Mater. Sci. Mater. Electron.*, vol. 31, no. 13, pp. 10 105–10 112, 2020.

[34] S. Sun et al., “Misorientations and subgrains in sn–ag and sn–ag–cu solder balls after solidification,” *J. Electron. Mater.*, vol. 53, no. 12, pp. 8024–8038, 2024.

[35] J. W. Xian et al., “The role of microstructure in the thermal fatigue of solder joints,” *Nat. Commun.*, vol. 15, no. 1, p. 4258, 2024.

[36] J. Wang et al., “Study on low silver sn–ag–cu–p alloy for wave soldering,” in *Proceedings of IEEE IPFA*, 2013.

[37] A. M. El-Taher et al., “Microstructural and mechanical enhancements in sn–ag–cu solder alloys,” *J. Mater. Sci. Mater. Electron.*, vol. 36, 2025.

[38] L. Liu et al., “A dislocation density based micromechanical constitutive model for sn–ag–cu solder alloys,” *Mater. Res. Express*, vol. 4, no. 10, p. 106 506, 2017.

[39] H. Alnahari et al., “The effect of tartaric acid concentration on the structural, morphological and optical properties of cuo-fe2o3-mgo nanocomposite,” *Sana’a Univ. J. Appl. Sci. Technol.*, vol. 1, no. 2, 2023.

[40] M. Z. Yahaya et al., “Microstructural analysis of sn–ag–cu–tio2 composite solder alloy,” *Mater. Res. Express*, vol. 7, no. 1, p. 016 583, 2020.

[41] W.-S. Ko, J. S. Lee, and D.-H. Kim, “Atomistic simulations of ag–cu–sn alloys,” *J. Mater. Res.*, vol. 37, no. 1, pp. 145–161, 2022.

[42] S. A. M. McNair et al., “Effect of porosity on strain evolution in soldered pipes,” *J. Mater. Res. Technol.*, vol. 22, pp. 2409–2424, 2023.

[43] D. Varanasi and M. K. Pal, “Density and viscosity of sn-based lead-free solders,” *Powder Metall. Met. Ceram.*, vol. 60, no. 7, pp. 504–512, 2021.

[44] M. I. Okereke and Y. Ling, “Void morphology and thermal resistance of solder tims,” *Appl. Therm. Eng.*, vol. 142, pp. 346–360, 2018.

[45] S. A. Alarnoot, A. H. Al-Hammadi, and A. M. A. Haider, “Zinc-induced effects on the structural and morphological properties of sn–zn–in triple alloys: Insights from xrd, edx, and sem analysis,” *Sana’a Univ. J. Appl. Sci. Technol.*, vol. 3, no. 4, pp. 922–932, 2025.

[46] S. Wang et al., “Critical review of size effects on solder joints,” *Appl. Sci.*, vol. 9, no. 2, p. 227, 2019.

[47] A. A. El-Daly and A. E. Hammad, “High-strength sn–0.7cu solders with ag and in,” *J. Alloy. Compd.*, vol. 509, no. 34, pp. 8554–8560, 2011.

[48] M. S. Gumaan, “Chromium effects on eutectic sn–ag alloy,” *J. Mater. Sci. Mater. Electron.*, vol. 31, no. 13, pp. 10 731–10 737, 2020.

[49] J. I. Goldstein et al., *Scanning Electron Microscopy and X-ray Microanalysis*, 4th ed. Springer, 2017.

[50] Y. M. S. Jamil et al., “The characterization, antibacterial and antioxidant of phytosynthesized zinc oxide nanoparticles using aloe fleurentinorum leaves extract,” *Sana’a Univ. J. Appl. Sci. Technol.*, vol. 2, no. 4, pp. 339–347, 2024.

[51] Y.-G. Kong et al., “Microstructure and mechanical property of sn–ag–cu solder material,” *Rare Met.*, vol. 36, no. 3, pp. 193–197, 2017.

[52] L. Zhang et al., “Microstructures and interface reaction of sn–ag–cu solders,” *J. Mater. Sci. Mater. Electron.*, vol. 31, no. 9, pp. 6645–6653, 2020.

[53] M. K. Pal et al., “Microstructural investigations and mechanical properties of lead-free solder alloys,” *Metall. Mater. Eng.*, vol. 24, no. 1, pp. 27–36, 2018.

[54] S.-K. Seo et al., “Microstructure and microhardness of sn-based solders,” *J. Electron. Mater.*, vol. 38, no. 2, pp. 257–265, 2009.

[55] E. M. A. Nassar, A. H. Al-Hammadi, and Y. H. I. Mohammed, “Morphological and optical analysis of α-al$_2$o$_3$:zn nanoparticles,” *Sana’a Univ. J. Appl. Sci. Technol.*, vol. 3, no. 6, pp. 1408–1418, 2025.

©2026 JAST